

# Chapter 7

## Transformation Electromagnetics Design of All-Dielectric Antennas

Wenxuan Tang and Yang Hao

**Abstract** The discrete coordinate transformation is a practical implementation of transformation electromagnetics. It solves the transformation between coordinate systems in a discretized form. This method significantly relaxes the strict requirement for transformation media, and consequently leads to easily-realizable applications in antenna engineering. In this chapter, the discrete coordinate transformation is demonstrated and analyzed from the theory and is proved to provide an all-dielectric approach of device design under certain conditions. As examples, several antennas are presented, including a flat reflector, a flat lens, and a zone plate Fresnel lens. The Finite-Difference Time-Domain (FDTD) method is employed for numerical demonstration. Realization methods are also discussed, and a prototype of the carpet cloak composed of only a few dielectric blocks is fabricated and measured.

### 7.1 Introduction

The concept of transformation electromagnetics was first proposed in 2006 in pioneering theoretical works by Leonhardt and Pendry et al. independently [1, 2]. It provides us with a flexible method to manipulate the propagation of electromagnetic waves by using custom-engineered media. Novel functional devices have been successfully proposed and designed through transformation electromagnetics, such as the exotic ‘cloak of invisibility’ [3–6], EM rotators [7, 8], EM concentrators [9–11], sensor cloaks [12], optical black holes [13, 14], antenna devices

---

W. Tang · Y. Hao (✉)  
School of Electronic Engineering and Computer Science, Queen Mary,  
University of London, London E1 4NS, United Kingdom  
e-mail: yang.hao@eecs.qmul.ac.uk

W. Tang  
State Key Laboratory of Millimeter Waves, Southeast University,  
Nanjing 210096, People’s Republic of China

[15, 16], etc. However, there exist considerable problems when transformation-based devices are put into practice. One such problem is that those designs often include extreme values of constitutive parameters (e.g., near zero or extremely high permittivity or permeability). Even though metamaterials have been proved to be capable of providing a wide range of permittivity and permeability and even to achieve extreme values, they often require resonant unit cells which severely limit the operating bandwidth. In addition, many transformation-based devices require anisotropic permittivity and permeability simultaneously, which makes their practical realization even more difficult.

The discrete coordinate transformation (DCT) is therefore proposed to circumvent these problems [17]. Instead of global coordinates, the physical space and the virtual space are described with quasi-orthogonal local coordinates, and the transformation electromagnetics equations are applied between a pair of corresponding local coordinate systems in the two spaces. A well-known application of the DCT technique is the ‘carpet cloak’. As demonstrated in [17], the carpet cloak can be constructed with conventional isotropic dielectrics instead of resonant metamaterials, and consequently overcomes the disadvantage of its narrow-band performance. Experimental validations of the carpet cloak have been done using low-loss and non-resonant artificial materials at microwave frequencies [18, 19] and at optical frequencies [20, 21].

Due to its easy realization and the broadband performance of the DCT based design, there are many possible applications other than the carpet cloak. For example, in antenna systems, many widely used devices have curved surfaces, such as parabolic reflectors and convex lenses. Using the discrete coordinate transformation, one can design equivalent devices that operate in the same manner but have flexible profiles. In the virtual space perceived by the electromagnetic waves, those devices have curved surfaces, contain homogeneous and isotropic materials, and can be described with distorted coordinate systems. By using appropriate transformations, these distorted coordinate systems are mapped to a physical space where the devices possess flat surfaces, contain spatially dispersive but isotropic materials, and are represented in new coordinate systems, for example, the Cartesian coordinate system.

The organization of this chapter is as follows: in Sect. 7.2, we begin with the theory of the discrete coordinate transformation, and give analyses towards its conditions of application. In Sect. 7.3, some examples of antenna devices are presented and numerically demonstrated. In Sect. 7.4, realization methods are discussed and a prototype of an all-dielectric device is fabricated and measured. A Summary of the above is in Sect. 7.5.

## 7.2 The Discrete Coordinate Transformation

To implement the discrete coordinate transformation, both the virtual space and the physical space are discretized into small cells using quasi-orthogonal local coordinate systems. For illustrative purpose we show in Fig. 7.1 an example of

transforming a parabolic reflector in the virtual space into a flat one in the physical space.

Suppose that the coordinate transformation between the virtual space (Fig. 7.1a) and the physical space (Fig. 7.1b) is  $x' = x'(x, y, z)$ ,  $y' = y'(x, y, z)$ ,  $z' = z'(x, y, z)$ , where  $(x, y, z)$  are local coordinates in the virtual space and  $(x', y', z')$  are local coordinates in the physical space. Based on the theory in [2], the permittivity and the permeability tensors in the physical space can be calculated as:

$$\bar{\bar{\epsilon}}' = \frac{J \bar{\bar{\epsilon}} J^T}{\det(J)}, \quad \bar{\bar{\mu}}' = \frac{J \bar{\bar{\mu}} J^T}{\det(J)}, \tag{7.1}$$

where the Jacobian matrix between each pair of local coordinate systems is

$$J = \begin{pmatrix} \frac{\partial x'}{\partial x} & \frac{\partial x'}{\partial y} & \frac{\partial x'}{\partial z} \\ \frac{\partial y'}{\partial x} & \frac{\partial y'}{\partial y} & \frac{\partial y'}{\partial z} \\ \frac{\partial z'}{\partial x} & \frac{\partial z'}{\partial y} & \frac{\partial z'}{\partial z} \end{pmatrix}. \tag{7.2}$$

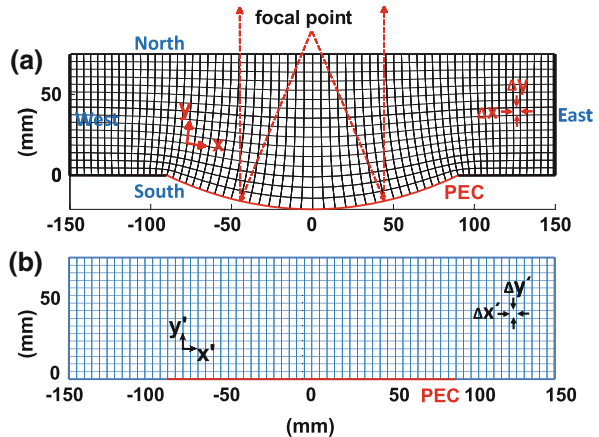
Because the parabolic reflector (shown as the curved PEC in Fig. 7.1a) is placed in the free space, the original permittivity and permeability tensors are

$$\begin{aligned} \bar{\bar{\epsilon}} &= \epsilon_0 \mathbf{I}, \\ \bar{\bar{\mu}} &= \mu_0 \mathbf{I}, \end{aligned} \tag{7.3}$$

where  $\mathbf{I}$  is the unitary matrix.

To simplify the problem, we assume that the transformation is two-dimensional (2D), and thus the device is infinite in the  $z$  direction normal to the  $x - y$  plane defined in Fig. 7.1. The bold reduction from three dimensions to two dimensions makes the design process much simpler. In practice, because many devices are symmetric, or work at a specified polarization, three-dimensional (3D) transformation devices can be obtained by rotating or extending 2D models about an axis.

**Fig. 7.1** (Section view)  
**a** The virtual space with distorted coordinates. A parabolic reflector is located in the free space, as illustrated by the curved PEC.  
**b** The physical space with Cartesian coordinates. The parabolic reflector is transformed into a flat PEC



Examples will be presented in [Sect. 7.3](#). For a 2D E-polarized incident wave with electric field along the  $z$  direction, only the components of  $\mu_{xx}$ ,  $\mu_{xy}$ ,  $\mu_{yy}$ ,  $\mu_{yx}$  and  $\varepsilon_{zz}$  contribute, and hence, the permittivity and the permeability become

$$\varepsilon'_z \equiv \varepsilon'_{zz} = \varepsilon_0 \det(J)^{-1}, \quad (7.4)$$

$$\bar{\mu}' = \frac{\mu_0}{\det(J)} \begin{pmatrix} \left(\frac{\partial x'}{\partial x}\right)^2 + \left(\frac{\partial x'}{\partial y}\right)^2 & \frac{\partial x'}{\partial x} \frac{\partial y'}{\partial x} + \frac{\partial x'}{\partial y} \frac{\partial y'}{\partial y} \\ \frac{\partial y'}{\partial x} \frac{\partial x'}{\partial x} + \frac{\partial y'}{\partial y} \frac{\partial x'}{\partial y} & \left(\frac{\partial y'}{\partial x}\right)^2 + \left(\frac{\partial y'}{\partial y}\right)^2 \end{pmatrix}. \quad (7.5)$$

Based on the theoretical study presented in [17], for anisotropic materials an effective average refractive index  $n'$  can be defined as

$$n'^2 = n'_{xx} n'_{yy} / (\varepsilon_0 \mu_0) = \sqrt{\mu'_{yy} \varepsilon'_z} \sqrt{\mu'_{xx} \varepsilon'_z} / (\varepsilon_0 \mu_0) = \sqrt{\mu'_{yy} \mu'_{xx} \varepsilon'_z} / (\varepsilon_0 \mu_0), \quad (7.6)$$

where  $\mu'_{xx}$  and  $\mu'_{yy}$  are the principal values of the permeability tensor in Eq. (7.5) and  $n'_{xx}$  and  $n'_{yy}$  are the corresponding principal values of the refractive index tensor.

Equation (7.6) indicates that if  $\mu'_{xx} \mu'_{yy} = \mu_0^2$ , i.e. if there is no magnetic dependence, then the refractive index  $n'$ , which determines the trace of the wave, can be realized by the permittivity alone, leading to an all-dielectric device. Next, we shall show that this condition is approximately satisfied if certain grids are properly chosen in the coordinate transformation.

The explicit value of  $\mu'_{xx} \mu'_{yy}$  from Eq. (7.5) is

$$\mu'_{xx} \mu'_{yy} = \mu_0^2 \frac{[(\frac{\partial x'}{\partial x})^2 (\frac{\partial y'}{\partial x})^2 + (\frac{\partial x'}{\partial x})^2 (\frac{\partial y'}{\partial y})^2 + (\frac{\partial x'}{\partial y})^2 (\frac{\partial y'}{\partial x})^2 + (\frac{\partial x'}{\partial y})^2 (\frac{\partial y'}{\partial y})^2]}{[(\frac{\partial x'}{\partial x})^2 (\frac{\partial y'}{\partial y})^2 - 2 \frac{\partial x'}{\partial x} \frac{\partial y'}{\partial y} \frac{\partial x'}{\partial y} \frac{\partial y'}{\partial x} + (\frac{\partial x'}{\partial y})^2 (\frac{\partial y'}{\partial x})^2]}. \quad (7.7)$$

According to Eq. (7.7), the approximate condition  $\mu'_{xx} \mu'_{yy} \simeq \mu_0^2$  is satisfied when at the same time

$$\frac{\partial x'}{\partial y} \simeq 0, \quad (7.8)$$

and

$$\frac{\partial y'}{\partial x} \simeq 0. \quad (7.9)$$

Since  $x'$  and  $y'$  are functions of both  $x$  and  $y$ , Eqs. (7.8) and (7.9) can be also written using the chain rule as

$$\frac{\partial x'}{\partial y} = \frac{\partial x'}{\partial x} \frac{\partial x}{\partial y} \simeq 0, \quad (7.10)$$

$$\frac{\partial y'}{\partial x} = \frac{\partial y'}{\partial y} \frac{\partial y}{\partial x} \simeq 0. \quad (7.11)$$

The above condition can indeed be satisfied because we can generate a grid in the virtual space with quasi-orthogonal cells such that

$$\frac{\partial x}{\partial y} \simeq 0, \quad (7.12)$$

$$\frac{\partial y}{\partial x} \simeq 0. \quad (7.13)$$

To illustrate how this orthogonality restriction can be approximately satisfied, see for example the virtual space shown in Fig. 7.1a. A sample distorted cell is drawn in Fig. 7.2, and the  $2 \times 2$  covariant metric  $g$  is re-defined to characterize the distortion as [22–24]:

$$g = \begin{pmatrix} g_{11} & g_{12} \\ g_{21} & g_{22} \end{pmatrix}, \quad (7.14)$$

$$g_{ij} = \vec{a}_i \cdot \vec{a}_j \quad (i, j = 1, 2). \quad (7.15)$$

$\vec{a}_1$  and  $\vec{a}_2$  are the covariant base vectors defined in Fig. 7.2, and  $\theta$  is the angle between them. We quantify the orthogonality of the grid using the parameter  $\theta$  for each cell, defined through

$$\cos \theta = \sqrt{\frac{g_{12}g_{21}}{g_{11}g_{22}}}. \quad (7.16)$$

The distribution of the angle parameter  $\theta$  is plotted in Fig. 7.3 for the grid shown in Fig. 7.1a. We observe that in most cells,  $\theta$  is distributed around the  $90^\circ$  point, with a much smaller exception further away from  $90^\circ$ . The full width at half maximum (FWHM) index of the distribution is also measured from this plot, which is only  $1^\circ$ , indicating that most of the local coordinates are quasi-orthogonal. Thus, for a perfectly orthogonal grid,  $g$  is a unit matrix,  $\cos \theta = 0$ , FWHM = 0, and ultimately  $\mu'_{xx}\mu'_{yy} = \mu_0^2$ . And even for a quasi-orthogonal grid such as the one in Fig. 7.1a, these conditions can be approximately satisfied, yielding an all-dielectric device with very minor sacrifices in performance.

**Fig. 7.2** The covariant base vectors in a 2D distorted cell

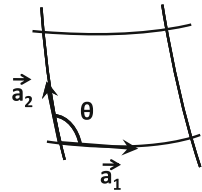
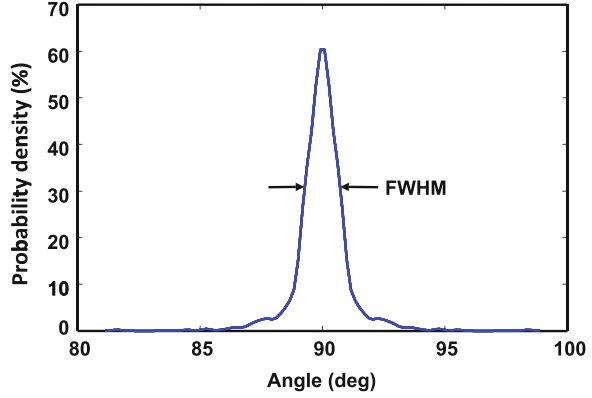


**Fig. 7.3** Distribution of the angle between two local coordinates in every cell of the virtual space. The orthogonal property is quantified by the full width at half maximum (*FWHM*) index. When the *FWHM* index approaches zero, the local coordinates are quasi-orthogonal. In this case the index is only  $1^\circ$



Furthermore, the near-orthogonal property ensures an approximation of Eq. (7.5) that

$$\bar{\mu}' = \frac{\mu_0}{\det(J)} \begin{pmatrix} \left(\frac{\partial x'}{\partial x}\right)^2 & 0 \\ 0 & \left(\frac{\partial y'}{\partial y}\right)^2 \end{pmatrix}. \quad (7.17)$$

Because all cells are generated to be approximately square-shaped,  $\mu'_{xx}$  and  $\mu'_{yy}$  have very similar values which are close to unity. Accordingly, the relative permeability of the device can be assumed to be isotropic and unity, and the effective relative refractive index in Eq. (7.6) is only dependent on  $\varepsilon'_z$  as

$$n'^2 \simeq \varepsilon'_z / \varepsilon_0 = \frac{1}{\det(J)}. \quad (7.18)$$

Note that under the orthogonal condition of Eqs. (7.8) and (7.9), the refractive index profile of the device can be directly retrieved from each cell within the grid, using Eq. (7.2):

$$n'^2 \simeq \frac{1}{\frac{\partial x'}{\partial x} \frac{\partial y'}{\partial y}} \simeq \frac{\Delta x \Delta y}{\Delta x' \Delta y'}, \quad (7.19)$$

where  $\Delta x$ ,  $\Delta y$ ,  $\Delta x'$ ,  $\Delta y'$  are the dimensions of cells in the two spaces, as marked in Fig. 7.1.

For the case of H polarization, similar results are obtained. Now the contributing components of the permittivity and the permeability are  $\varepsilon_{xx}$ ,  $\varepsilon_{xy}$ ,  $\varepsilon_{yy}$ ,  $\varepsilon_{yx}$  and  $\mu_{zz}$ . Under the orthogonality criteria of Eqs. (7.8) and (7.9), the permittivity and the permeability tensors become

$$\bar{\varepsilon}^J = \frac{\varepsilon_0}{\det(J)} \begin{pmatrix} \left(\frac{\partial x'}{\partial x}\right)^2 & 0 \\ 0 & \left(\frac{\partial y'}{\partial y}\right)^2 \end{pmatrix}, \mu'_z = \mu_0 \det(J)^{-1}, \quad (7.20)$$

while  $\det(J) = \frac{\partial x'}{\partial x} \cdot \frac{\partial y'}{\partial y}$ . The effective average refractive index is now

$$n^2 = n'_{xx}n'_{yy}/(\varepsilon_0\mu_0) = \sqrt{\varepsilon'_{yy}\varepsilon'_{xx}\mu'_z}/(\varepsilon_0\mu_0). \quad (7.21)$$

It can be easily checked that in this case  $\varepsilon'_{xx}\varepsilon'_{yy} \simeq \varepsilon_0^2$ , and thus the effective average refractive index in this case is dependent on  $\mu'_z$  only, similar to Eq. (7.18) as:

$$n^2 \simeq \mu'_z/\mu_0 = \frac{1}{\det(J)}. \quad (7.22)$$

The above analysis indicates that a properly selected magnetic material can control the H-polarized wave, similar to how a dielectric material can control the E-polarized wave. Thus the designer can generate a grid under the assumptions specified in this section, calculate the refractive index distribution from Eq. (7.19), and choose to tune either  $\varepsilon$  or  $\mu$  to operate using E-polarization or H-polarization respectively.

## 7.3 All-Dielectric Antennas Based on the Discrete Coordinate Transformation

### 7.3.1 A Flat Reflector

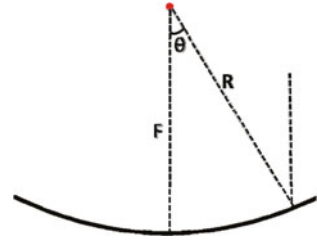
The parabolic reflector antenna is one of the most commonly used antennas from radio to optical frequencies [25]. This antenna serves to transform a spherical wave originated from its focal point into a plane wave, and consequently generates highly directive beams. Such an antenna device can be considerably large when operated at low frequencies, and difficult to construct due to the parabolic shape. In [26], the technique of discrete coordinate transformation was implemented to create an alternative to the parabolic reflector: an all-dielectric reflector that possesses a compact flat volume while maintaining the performance of the parabolic dish.

Figure 7.4a shows the geometry of a prototype of conventional parabolic reflector, whose shape follows the equation of

$$R = \frac{2F}{1 + \cos \theta}. \quad (7.23)$$

This parabolic reflector is designed to operate at the C-band (4–8 GHz) and the X-band (8–12 GHz). The focal length  $F$  is set to be 108.6 mm and the angle  $\theta$  ranges from  $-45^\circ$  to  $45^\circ$ . Accordingly, the aperture of the parabolic surface is 180 mm. This parabolic reflector is exactly the same as the one located in Fig. 7.1a. It is noted that in Fig. 7.1a the transformation region is chosen to be 300 mm  $\times$  75 mm, so as to ensure that in the physical space in Fig. 7.1b a source placed at the focal

**Fig. 7.4** Geometry of the parabolic reflector located in Fig. 7.1a



point is not embedded in the transformation media. Quasi-orthogonal grids are generated in both the virtual space and the physical space as illustrated in Fig. 7.1, using a commercial software called ‘PointWise’ [27]. Based on the analysis in previous section, these grids are indeed quasi-orthogonal, leading to an all-dielectric flat reflector in the physical space. The permittivity distribution of the transformation based flat reflector is calculated according to Eqs. (7.18) and (7.19). The complete permittivity map is shown in Fig. 7.5a, consisting of  $64 \times 16$  square blocks.

To reduce the complexity of the flat reflector and to make it more realizable, some simplifications are adopted. First, materials with relative permittivity of less-than-unity value are neglected and replaced with those of  $\epsilon_r = 1$  as air or free space. In this design, materials with less-than-unity permittivities are found close to the bottom around  $x = 80$  mm and  $x = -80$  mm (see Fig. 7.5a). Since these areas are electrically small at operating frequencies, and those permittivity values are often very close to one, the simplification is considered to be safe. This fact has been demonstrated in Refs. [19, 26, 28], and will be shown later by simulation results in this section. The permittivity map without less-than-unity values is shown in Fig. 7.5b. It should be pointed out that materials with less-than-unity parameters are termed as ‘dispersive materials’ here, as they are strongly dispersive over operating frequencies. Strictly speaking, all materials are essentially dispersive in frequency. However, conventional dielectrics can be nearly non-dispersive at the X-band and the C-band [19].

The second step to approximate and simplify the transformation device is to reduce the resolution of permittivity map. This concept has been developed in the design of a simplified carpet cloak made of only a few blocks of isotropic all-dielectric materials [19, 29]. The fundamental limitation of resolution is based on the Nyquist-Shannon sampling theorem [30]. Sampling is the process of converting a signal (for example, a function of continuous time or space) into a numeric sequence (a function of discrete time or space). Shannon’s version of the theorem states: *If a function  $f(t)$  contains no frequencies higher than  $W$  cps, it is completely determined by giving its ordinates at a series of points spaced  $1/2W$  seconds apart.* Fig. 7.6 interprets this theorem in the spatial domain. When propagating in the physical space, at a fixed time, the electromagnetic wave is a function of continuous space. Transformation media with a high resolution discretize the space using a high sampling rate while low-resolution ones discretize the space using a low sampling rate. If the electromagnetic wave operates in a



**Fig. 7.5** **a** Relative permittivity map consisting of  $64 \times 16$  blocks. **b** Relative permittivity map consisting of  $64 \times 16$  blocks, without less-than-unity values. **c** Relative permittivity map consisting of  $16 \times 3$  blocks. **d** Relative permittivity map consisting of  $16 \times 3$  blocks, without less-than-unity values

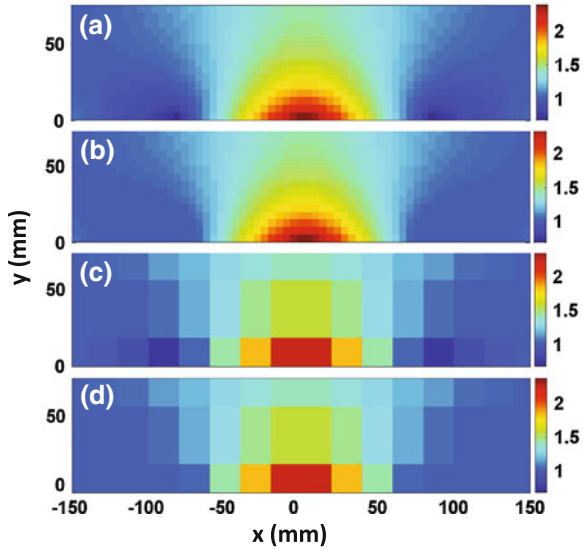
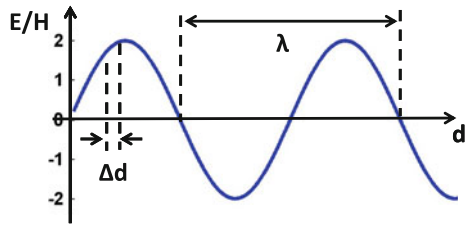


**Fig. 7.6** An electromagnetic wave propagates in the spatial domain at a fixed time



frequency band from  $f_L$  to  $f_H$ , to accurately reconstruct information of the wave, the sampling rate  $f_s$  should satisfy

$$f_s > 2f_H. \tag{7.24}$$

Because

$$f_s = \frac{1}{\Delta d}, f = \frac{1}{\lambda}, \tag{7.25}$$

the resolution of the discrete space should satisfy

$$\Delta d < \frac{1}{2} \lambda_H. \tag{7.26}$$

$\Delta d$  is presented as the dimension of blocks in the permittivity map, and  $\lambda_H$  is the minimum wavelength within the frequency band. According to Eq. (7.26), as long as dielectric blocks are smaller than half a wavelength at operating frequencies, the simplified device can maintain the property of a high-resolution one. When the

operating frequency goes higher, the resolution of the permittivity map should increase accordingly.

The above simplifications have made significant advances for the transformation device to be able to be realized in practice. When applied to the present work, the high resolution permittivity map shown in Fig. 7.5a thus can be approximated using a relatively low resolution map of  $16 \times 3$  blocks as shown in Fig. 7.5c. The size of each block is 18.75 mm, which is half a wavelength in free space at 8 GHz. To execute the simplification, the position of a block in Fig. 7.5a–d is defined as the position of its center point. Each low-resolution block in figure c/d can find a high-resolution one in figure a/b which has the closest position to it. Once the two blocks are decided, the permittivity in the high-resolution block is filled into the low-resolution one uniformly. Figure 7.5d shows the simplified map without values less than unity (we call it a ‘non-dispersive map’ in the following text).

The FDTD method based simulations are employed to compare the performance of the parabolic reflector and the flat reflector [31, 32]. For simplicity, we use 2D modelling with  $H_x$ ,  $H_y$  and  $E_z$  components (E polarization). A 3D reflector is easily realizable by rotating the permittivity map in Fig. 7.5 to the  $y$  axis. For the reflector in this design, the simulation domain is relatively small and a conventional Cartesian grid is fine enough to accurately model the device. A spatial resolution of  $\lambda/30$  is chosen for the FDTD grid. The total-field/scattered-field technique is applied to implement an incident plane wave. Perfectly matched layer (PML) absorbing boundary conditions are added surrounding the antennas in order to terminate the simulation domain. Dispersive modelling [33, 34] is also employed to simulate the full-mapped flat reflector with less-than-unity values.

First, a plane wave with E polarization comes along  $+y$  direction at 8 GHz, in order to compare the low-resolution non-dispersive flat reflector shown in Fig. 7.5d with the parabolic reflector in term of the focal length. Figure 7.7a and b illustrate the real part of the  $E_z$  field from the transformed flat reflector and the conventional parabolic reflector, respectively, after the steady-state is reached. Their focal lengths are measured as the distances from the center of the PEC surface to the narrowest envelope marked with the dashed red line in Fig. 7.7a and b. The focal lengths in Fig. 7.7a and b are 102.6 and 102.7 mm respectively, very close to each other. In addition, slightly different reflections are observed on two sides of the reflectors. This difference is due to the neglecting of less-than-unity permittivities, and the discontinuity between the flat reflector and the air. In Fig. 7.7c and d we also compare the performance of these two reflectors when fed by a small horn with its phase center located at the focal point. The field distributions illustrated are indeed similar, which indicates that the flat reflector maintains the function of transforming an incident cylindrical wave to a plane wave and consequently obtains highly directive beams.

To investigate the directive property of the antennas, in Fig. 7.8 radiation patterns of the conventional reflector, flat reflectors with different resolutions, and the radiation pattern of a flat PEC surface alone, are compared. The near-to-far-field (NTFF) transformation is applied to observe the far-field characteristics [31].

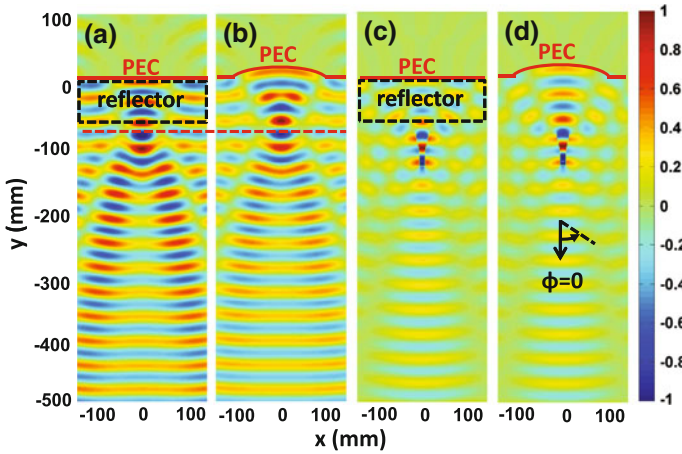


**Fig. 7.7** Real part of the  $E_z$  field at 8 GHz. **a** A plane wave along the  $y$  direction illuminates a low-resolution flat reflector shown in Fig. 7.5d. The focal length (measured from the *dashed red line* to the *center* of the PEC) is 102.6 mm. **b** The same plane wave illuminates the conventional parabolic reflector. The focal length is 102.7 mm. **c** A small horn antenna is applied at the focal point to feed the flat reflector. **d** A small horn antenna is applied at the focal point to feed the conventional reflector

Using the data obtained from the near-field simulation, the NTF transformation calculates the forward radiation patterns of the reflectors. The energy is calculated as  $|E_z|^2$ , and normalized to the peak energy when the conventional reflector is applied. It is shown in Fig. 7.8 that the conventional reflector and all the three flat reflectors produce highly directive beams around  $\phi = 0$  ( $\phi$  defined in Fig. 7.7d), which verifies the excellent cylindrical-to-plane wave transformation. The  $64 \times 16$ -block flat reflectors, dispersive (with less-than-unity permittivities) or non-dispersive (without less-than-unity permittivities), seem to have insignificant energy loss around the radiating direction when compared to the conventional parabolic one. In addition, when the less-than-unity values are removed from the full  $64 \times 16$  map, the performance deteriorates only slightly, in term of the energy reduction around  $\phi = 0$ . Once the  $16 \times 3$ -block map is applied, the flat reflector suffers more energy loss in the radiating direction. However, its directive property is still comparable to that of the conventional reflector. When all reflectors are removed, obviously, the PEC surface alone cannot hold the directive property.

Furthermore, the bandwidths of the dispersive and non-dispersive flat reflectors are tested at different frequencies. Both the flat reflectors are composed of  $16 \times 3$  large blocks, and the testing frequencies are 4, 6, 10 and 12 GHz respectively. Figure 7.9 shows that at frequencies higher than 8 GHz, the two reflectors have extremely similar radiation patterns. When the operating frequency goes lower, the dispersive reflector has higher radiation around the angle of  $\phi = 0$ , but slightly larger side-lobes than the non-dispersive one. This effect occurs since as the

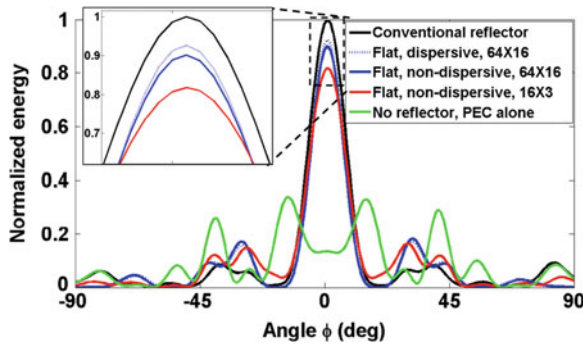


Fig. 7.8 The comparison of the radiation patterns at 8 GHz. The definition of  $\Phi$  is shown in Fig. 7.7d

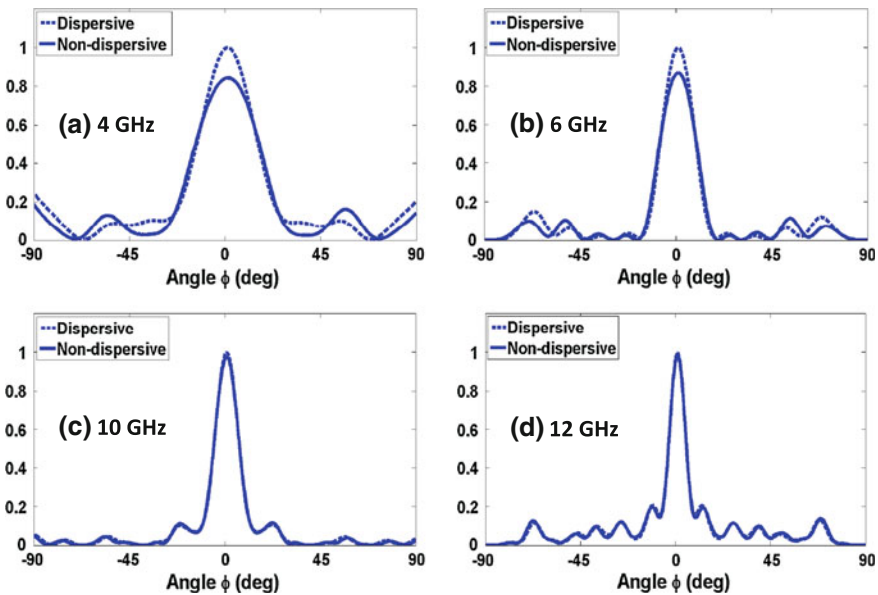


Fig. 7.9 Comparison of the radiation patterns between dispersive and non-dispersive flat reflectors at 4, 6, 10 and 12 GHz. Both the flat reflectors are composed of  $16 \times 3$  blocks

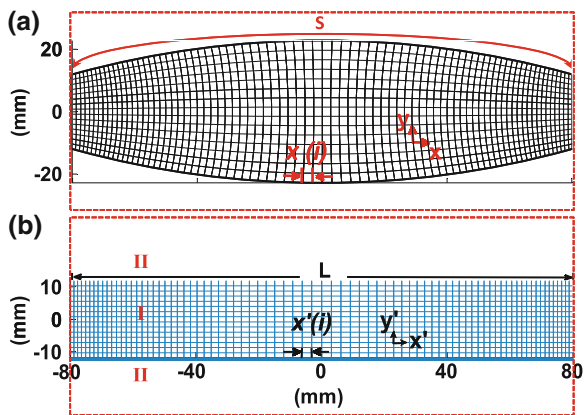
operating frequency decreases, the less-than-unity values change more and more rapidly according to the Drude model. In conclusion, a non-dispersive reflector has a comparable radiating performance and a wider bandwidth than the dispersive one, and is much easier to realize.

### 7.3.2 A Flat Lens

A convex lens is another common device in antenna systems. It functions to transform a spherical wave from a point source (or a cylindrical wave from a line source in a 2D problem) located at its focal point to a plane wave at the other side. This device has been widely used at different frequencies and at various polarizations. In [26], an all-dielectric lens at the C-band and the X-band was created from a conventional convex lens by using the discrete coordinate transformation. The created lens obtained very similar performance as the convex one, whilst possessing a planar profile with half the thickness of the other one.

Figure 7.10a shows the section view of the virtual space where the original convex lens is located. It is supposed to be made of isotropic homogeneous dielectric with  $\epsilon_r = 3$ . The aperture of the lens is 160 mm ( $4.3 \lambda_0$  at 8 GHz), and the two surfaces are arcs on a circle with radius equal to 300 mm. The thickness varies from 45.6 to 23.8 mm, from the center ( $x = 0$ ) to the two ends ( $x = \pm 80$  mm). Applying the discrete coordinate transformation, the conventional convex lens in the virtual space is completely compressed into the flat physical space with half the thickness, as shown in Fig. 7.10b. Contrary to the boundary condition in the flat reflector design, here the top and bottom boundaries in the virtual space are curves. Since the boundaries are different before and after the transformation, if we want to grant the transformation lens exactly the same property as the conventional one, we should add transformation media surrounding the flat profile (filling region II in Fig. 7.10b) in order to maintain the space and to palliate the impedance mismatching [35]. Unfortunately, such filling materials commonly have some permittivity values less than the unity, which results in narrow-band performance. In addition, if we fix the boundaries before and after transformation, the flat lens will lose the benefit of small volume. It is obvious that both of the above two factors are important to a broadband antenna. Therefore, we can assume that firstly a complete virtual space with air surrounding the convex lens (within the dashed red box in Fig. 7.10a) is transformed to a physical space (within the dashed red box

**Fig. 7.10** **a** The virtual space with distorted coordinates. A convex lens made of dielectric with  $\epsilon_r = 3$  is imbedded in the air. **b** The physical space with Cartesian coordinates. The transformation lens is inside region I



in Fig. 7.10b), and then materials with less-than-unity parameters in the physical space are replaced with the air. Therefore, the flat lens in the physical space can have a compact size and potentially broadband performance. As long as the performance is properly maintained, as will be proved, this approximation is valid in practice.

Quasi-orthogonal grids are again generated to discretize both the virtual space and the physical space. In the virtual space, to achieve a good orthogonality, points on the top and bottom boundaries are no longer evenly distributed. More points assemble at the four corners, resulting in smaller cells at the two ends and larger cells in the central area. In the physical space, the points on the top and bottom boundaries are determined in the same proportion as that in the virtual space because  $x'$  is the projection of  $x$ . Note that since some cells in the physical space are not squares, the components of  $\mu_{xx}$  and  $\mu_{yy}$  have different values, implying that the transformation media in the physical space have become more anisotropic. Strictly speaking, the effective average refractive index has approximate values of  $n^2 \simeq \frac{1}{\det(J)}$  in the central area and at the two ends. Nevertheless, for a near-axis incidence, the isotropic approximation is acceptable, and the flat lens holds its performance, as will be demonstrated later. The covariant metric  $g$  is calculated for each cell, and the FWHM index is  $3.6^\circ$ , indicating that local coordinate systems are fairly orthogonal and the discrete coordinate transformation can be applied.

In Fig. 7.11 the permittivity maps with different resolutions are presented, calculated by Eqs. (7.18) and (7.19). The high-resolution map in Fig. 7.11a is composed of  $80 \times 15$  blocks, with each block sized about  $2 \text{ mm} \times 1.7 \text{ mm}$ . Proper simplification is implemented to reduce the resolution using the same technique described in the previous sub-section, and a low resolution permittivity map is exhibited in Fig. 7.11b, consisting of  $14 \times 2$  blocks sized  $12.3 \text{ mm} \times 11.9 \text{ mm}$ . It is noted that the two rows of blocks have the same permittivity values, therefore the low-resolution map is in fact composed of  $14 \times 1$  blocks.

The FDTD method based simulations are employed again to predict the performance of the designed flat lens in a 2D E-polarized circumstance. In Fig. 7.12 the real part of the electric field under different excitations are depicted. To test the focusing property of the  $14 \times 1$ -block low-resolution lens, we compare the field

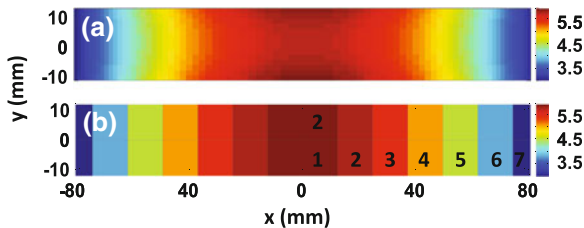
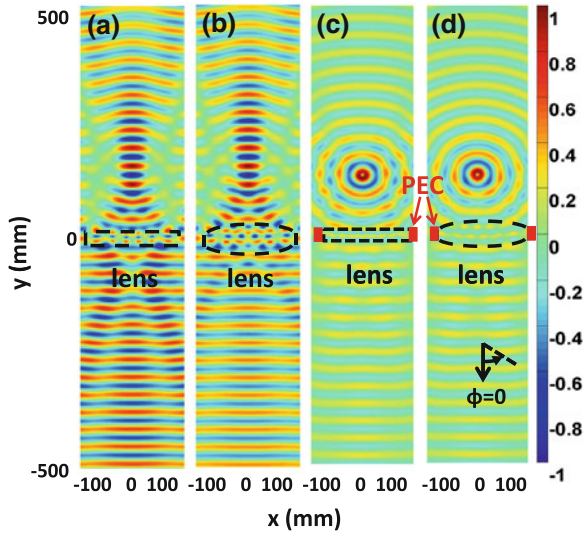


**Fig. 7.11** Permittivity maps of the flat lens. **a** The map consisting of  $80 \times 15$  blocks, with each block sized  $2 \times 1.7 \text{ mm}$ . **b** The map consisting of  $14 \times 2$  blocks. The first and last columns have a width of  $6.2 \text{ mm}$  and the rest have a width of  $12.3 \text{ mm}$

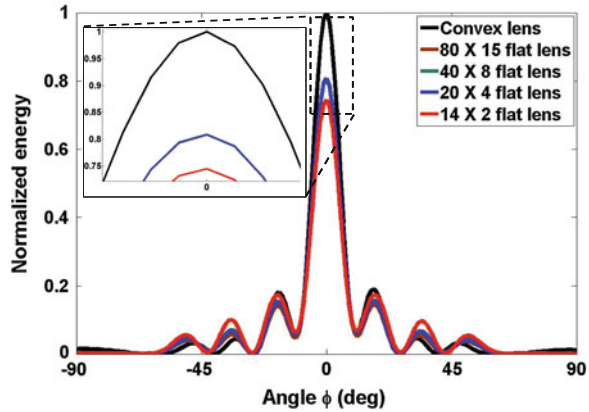
**Fig. 7.12** The real part of the  $E_z$  field at 8 GHz. **a** A plane wave illuminates the low-resolution flat lens from the bottom. The focal length is 130 mm. **b** The same plane wave illuminates the conventional lens from the bottom. The focal length is 131 mm. **c** A line source is located at the focal point to feed the low resolution flat lens. **d** A line source is located at the focal point to feed the conventional lens



distribution when a plane wave is applied to illustrate the flat lens and the convex lens in Fig. 7.12a and b respectively. The focal length is measured from the center of the lens to the point with the maximum amplitude. The flat lens has a focal length of 130 mm, whilst the conventional convex lens has a focal length of 131 mm. Apparently, the two lenses focus energy to almost the same position, even though their profiles are quite different. Next, line sources are placed on the focal points of the two lenses in order to generate plane waves on the other side. Two blocks of PEC are added to the left and right sides of the lens to prevent interference from leaky waves. Figure 7.12c and d depict the real parts of the  $E_z$  field when the low-resolution flat lens and the conventional lens are used, respectively. Indeed, plane waves are seen to emerge on the other side, which verifies the excellent performance of the simplified all-dielectric flat lens. Note also that the reflected waves are stronger on the side of  $y > 0$  when the flat lens is applied. This is because blocks with large permittivity values are located in the central area of the flat lens, causing a stronger impedance mismatch to the air.

To test the relationship between the resolution and the antenna performance, in terms of the radiation pattern and the bandwidth, two additional permittivity maps with  $40 \times 8$  blocks and  $20 \times 4$  blocks are also generated (but are not given in Fig. 7.11). Since all these flat lenses are expected to operate from 4 to 12 GHz, the minimum wavelength is calculated at 12 GHz. In the transformation media, the average relative permittivity is about 5, therefore half the minimum wavelength is about 5.6 mm. It is apparently that blocks in the  $80 \times 15$ -block map and in the  $40 \times 8$ -block map are smaller than half the wavelength, which means that both resolutions are fine enough according to the sampling theorem. Blocks in the  $20 \times 4$  map are slightly bigger than half the wavelength. This reduced resolution may harm the performance, but not significantly. The  $14 \times 1$ -block map has an

**Fig. 7.13** Comparison of the radiation patterns at 8 GHz. The definition of  $\Phi$  is shown in Fig. 7.12d



unqualified resolution, which will result in obvious degradation to the performance.

To prove the above assumption, the radiation patterns of the conventional lens and the four flat lenses with different resolutions are depicted in Fig. 7.13. When the permittivity map decreases from  $80 \times 15$  blocks to  $40 \times 8$  blocks and then to  $20 \times 4$  blocks, the performance remains almost unchanged at 8 GHz. In the radiating direction of  $\phi = 0^\circ$ , the three curves are exactly the same. The  $20 \times 4$ -block map has slightly increased side lobes compared with the other two. However, it can be considered as the threshold resolution. A visible degradation is observed when the map reduces to  $14 \times 1$  blocks. The energy validated in the direction of  $\phi = 0^\circ$  drops to about 75 % ( $-1.25$  dB) of that from a convex lens, accompanied with an obvious increase of side lobes. Although its performance is acceptable for many applications in practice, theoretically speaking, the properties of a propagating wave are not accurately re-constructed under this resolution. In Fig. 7.14, the radiation patterns are also tested at 4, 6, 10 and 12 GHz, respectively. Again, the  $20 \times 4$ -block map is proved to have almost the same performance as the  $80 \times 15$ -block map, indicating the resolution is adequate. As the operating frequency increases, the  $14 \times 1$ -block map brings in lower radiation around  $\phi = 0^\circ$  and different side lobes. However, from an engineering point of view, the  $14 \times 1$ -block flat lens operates effectively in a broad frequency band from 4 to 12 GHz.

Since the created flat lenses are made of isotropic dielectrics, a 3D model is straightforwardly accomplished by rotating a 2D model about its optical axis, as illustrated in Fig. 7.15. It has been demonstrated in 2D simulations that the  $20 \times 4$ -block map is a considerable threshold with a qualified resolution, whilst the  $14 \times 1$ -block map has an unqualified resolution. Accordingly, their 3D models are tested to further prove the relationship between performance and resolution. The commercial software, Ansoft HFSS [36], is applied as another tool for numerical simulation. An electric dipole is located at the focal point to generate an



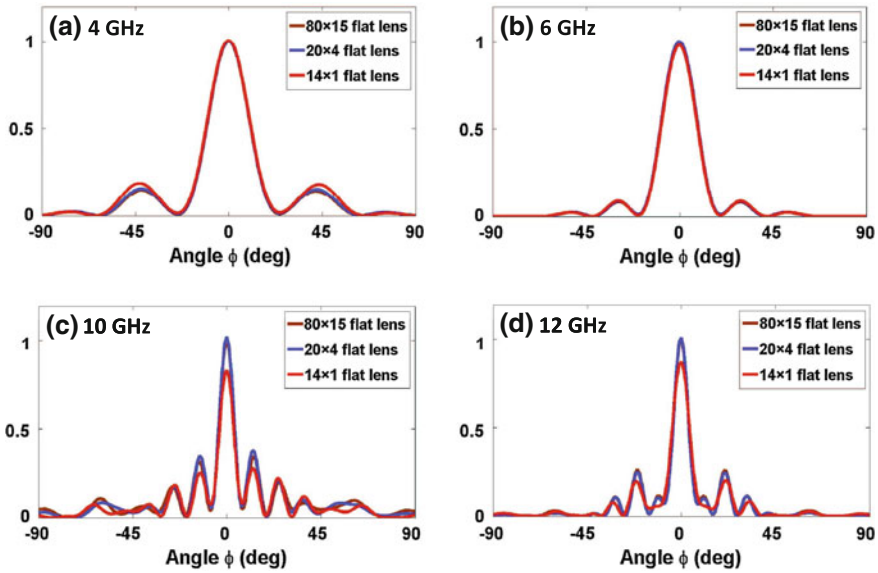


**Fig. 7.14** Comparison of the radiation patterns when the flat lenses are fed by a line source at focal points. Three lenses with different resolutions ( $80 \times 15$  blocks,  $20 \times 4$  blocks and  $14 \times 1$  blocks) are tested at 4, 6, 10 and 12 GHz respectively

incident Hertzian-Dipole wave, and the directive property of both two flat lenses and the convex lens are compared.

Figure 7.16a–c present the directivity patterns of the three lenses in both the E-plane and the H-plane at 4, 8 and 12 GHz, respectively. At 4 GHz, when the resolution of the  $14 \times 1$ -block lens is similar to half the wavelength, the  $14 \times 1$ -block lens has almost the same directivity as the  $20 \times 4$ -block one. When the frequency increases to 8 GHz, the two lenses still have very similar directivity patterns. The lower-resolution one has slightly lower peak directivity (the maximum directivity over all the directions, as defined by HFSS), and slightly increased side lobes. As the operating frequency further increases to 12 GHz, the difference between the two lenses enlarges. The peak directivity of the low-resolution lens decreases further and the side lobes increase as well. However, the low-resolution lens still holds a good directivity pattern, which agrees well with the results from 2D simulations. Besides, the convex lens always has the best directivity in terms of the highest peak directivity and the lowest side lobes.

Figure 7.16d plots the peak directivity of the three lenses from 2 to 16 GHz, so as to compare their operating bandwidth. The convex lens has a  $-3$  dB bandwidth from about 8.5 GHz to about 16.7 GHz (8.2 GHz span), the  $20 \times 4$ -block lens has a bandwidth from about 7.7 GHz to about 16 GHz (8.3 GHz span), and the  $14 \times 1$ -block lens has a bandwidth from about 6.6 GHz to about 15.5 GHz (8.9 GHz span). Overall, in the entire frequency band, the peak directivity decreases as the convex lens, the  $20 \times 4$ -block lens and the  $14 \times 1$ -block lens are applied respectively.

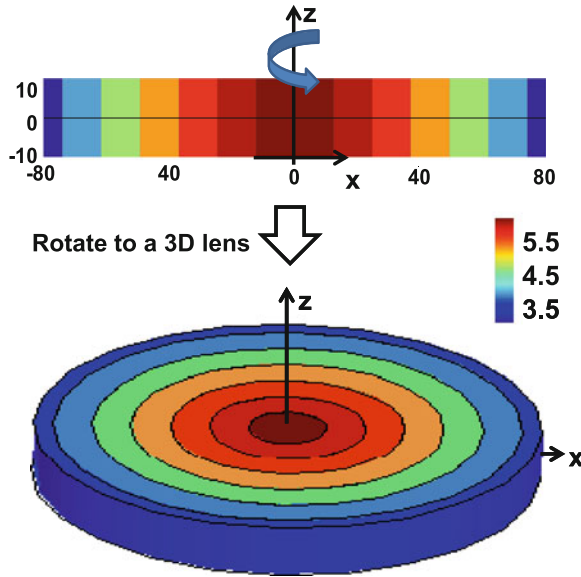


Fig. 7.15 A 3D flat lens is created by rotating the 2D permittivity map about its optical axis. The 3D lens is made of annular dielectric blocks. Colour bar shows the relative permittivity values

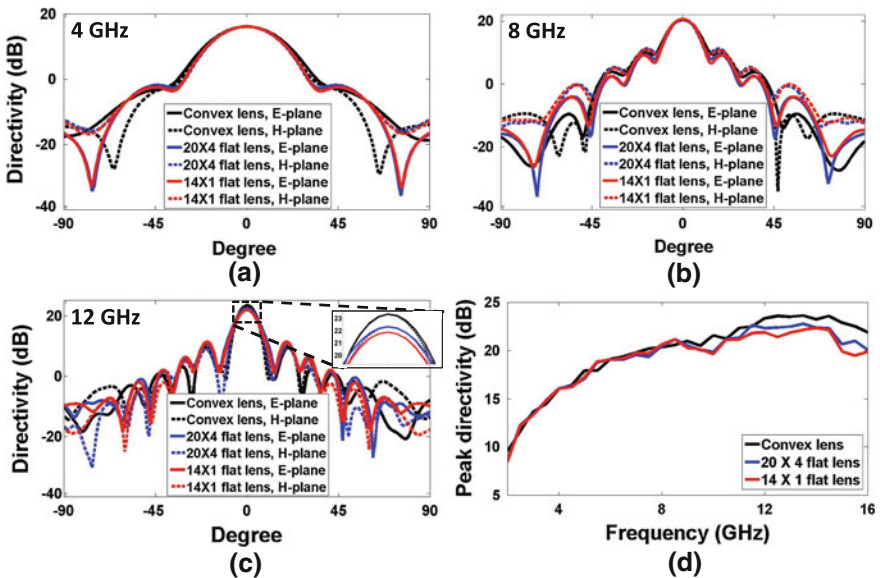
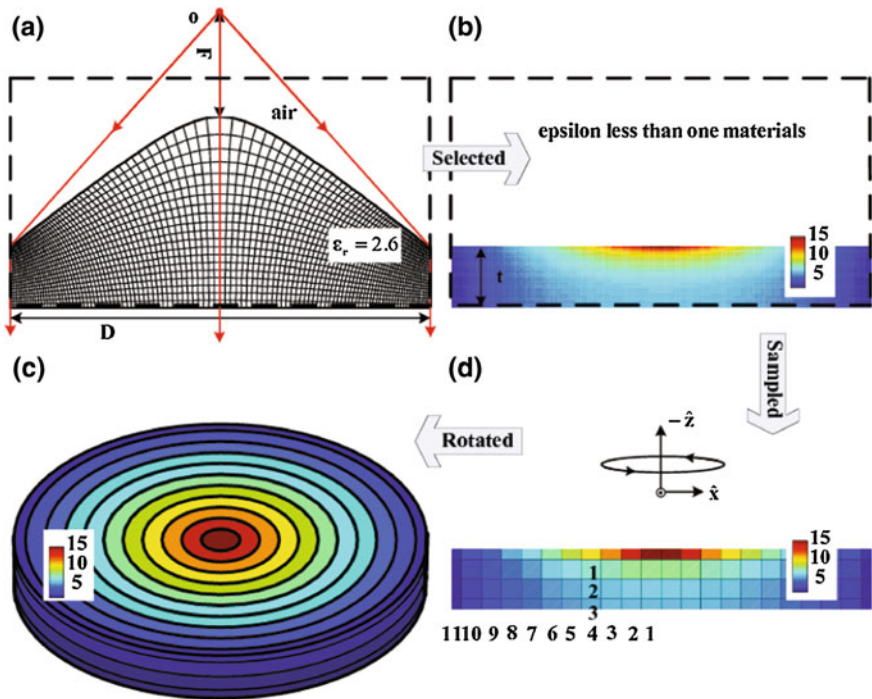


Fig. 7.16 Comparison of the directivity of the convex lens, the  $20 \times 4$ -block lens and the  $14 \times 1$ -block lens. The directivity patterns are drawn in the E-plane and the H-plane at **a** 4 GHz, **b** 8 GHz and **c** 12 GHz. In **d**, peak directivities of the three lenses are plotted from 2 to 16 GHz

The differences between the three lenses become larger as the operating frequency goes higher. It is also noted that at low frequencies, all three lenses have low directivity. The underlying physics is that when the aperture size of a lens is comparable to the wavelength, it cannot efficiently focus energy to the focal point, or reform the phase front of the wave.

### 7.3.3 A Broadband Zone Plate Lens

The diffractive lens, as an alternative to the traditional plano-convex lens for many optical applications, offers significantly reduced thickness with its flat profile, and thus possessing the merits of easy fabrication and small volume [37]. However, the tradeoff for such a low profile lens, based on the principle of wave diffraction instead of refraction, is narrow-band operation. For example, a Fresnel zone plate lens can obtain a very compact profile with its focal point being very close to the



**Fig. 7.17** Schematic showing of the zone plate lens design from the discrete coordinate transformation. **a** 2D hyperbolic lens in quasi-orthogonal coordinates. The parameters are  $D = 63.5$  mm,  $F = D/4$ ,  $t = 9$  mm. **b** 2D flat lens with the permittivity map consisting of  $110 \times 20$  blocks. **c** 2D flat lens with the permittivity map consisting of  $22 \times 4$  blocks. The four layers have heights of 1.4, 3, 3 and 1.6 mm respectively in the  $z$  direction. The 1st to 10th annular thickness is 3 mm and the 11th annular thickness is 1.75 mm. **d** The 3D zone plate lens

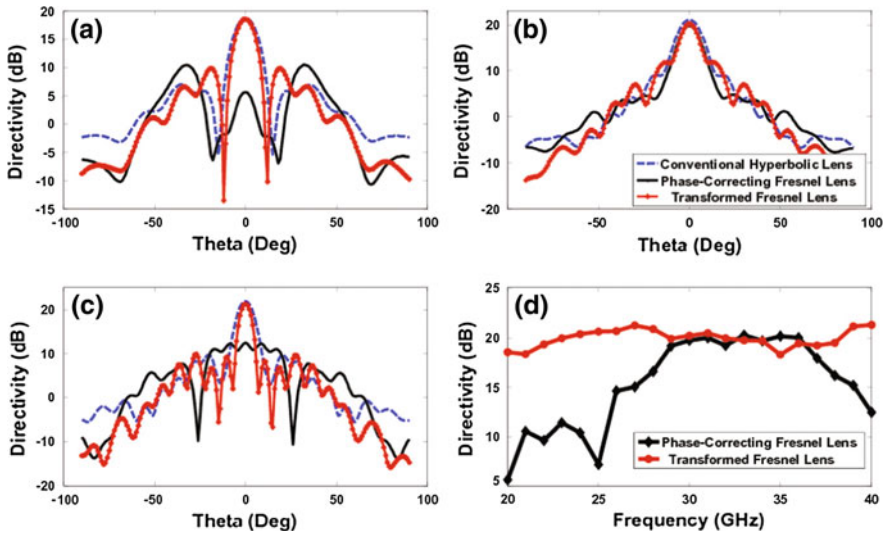
plate [38–40], but becomes incapable of performing phase correction when the operating frequency varies. In [41], a zone plate lens utilizing a refractive instead of diffractive approach was presented for broadband operation. Using the discrete coordinate transformation, a conventional hyperbolic lens was compressed into a flat one with a few zone plates made of all-dielectric materials. Such a transformed lens maintained the broadband performance of the original lens and achieved an effectively reduced volume, thus providing a superior alternative to the diffractive Fresnel element which is inherently narrow band.

Figure 7.17 is the schematic showing of the design procedure. A quasi-orthogonal grid is generated in the virtual space where the hyperbolic lens is located, as shown in Fig. 7.17a. Figure 7.17b illustrates the permittivity map in the physical space consisting of  $110 \times 20$  blocks. So far, a conventional hyperbolic lens in the virtual space has been completely compressed into the flat profile in the physical space, and hence the thickness of the lens is significantly reduced. After that, simplifications are again carried out, with the additional transformation layer in Fig. 7.17b neglected, and a low-resolution permittivity map ( $22 \times 4$  blocks) in Fig. 7.17d created. Finally, the 2D lens model is rotated to its optical axis and a 3D zone plate lens is therefore achieved in Fig. 7.17c.

A full-wave finite-element simulation using Ansoft HFSS is then performed to verify the proposed design. Three devices are simulated for comparison: the conventional hyperbolic lens, the transformed zone plate lens, and a quarter-wave phase-correcting Fresnel lens with the same aperture size  $D$  and the same thickness  $t$  as the zone plate lens. When a point source is placed on the focal point of each lens, all three lenses have high directivity and well-matched radiation patterns as expected at the designed central operating frequency of 30 GHz. The corresponding pattern for this scenario is shown in Fig. 7.18b. Compared with the original hyperbolic lens, the side lobes of the transformed lens become slightly higher, due to the simplification and approximation in the design. However, the transformed zone plate lens retains acceptable performance over a broad bandwidth from 20 to 40 GHz. In contrast, the phase-correcting Fresnel lens has a severely degraded directivity at both 20 and 40 GHz due to the phase error, as shown in Fig. 7.18a and c. Figure 7.18d further explores the bandwidth property of the phase-correcting Fresnel lens and the zone plate lens in term of directivity. The zone plate lens is proved to possess a steady performance over 20 to 40 GHz, while the phase correcting Fresnel lens only has 5 GHz bandwidth from 30 to 35 GHz.

## 7.4 Realization Methods

As pointed out in Sect. 7.2, constraints from less-than-unity permittivity or permeability have been completely removed in a device based on the discrete coordinate transformation. This fact significantly reduces the complexity of realizing a proposed design in practice, meanwhile grants the design with broadband performance because its composing material is no longer strongly dispersive in



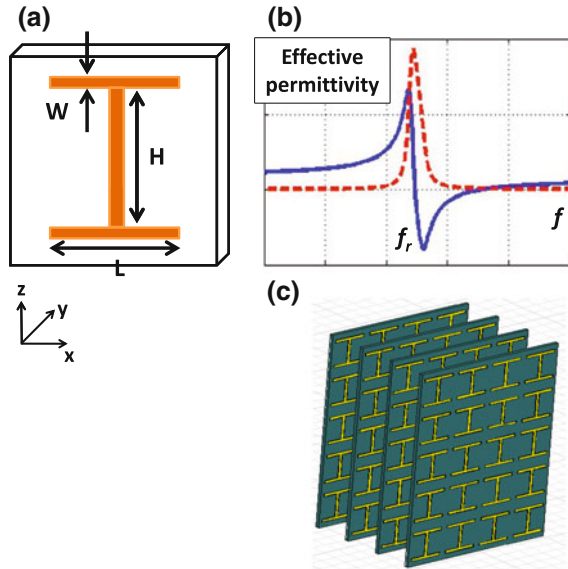
**Fig. 7.18** Radiation patterns of the conventional hyperbolic lens, the transformed zone plate lens and the phase-correcting Fresnel lens at **a** 20 GHz, **b** 30 GHz, and **c** 40 GHz. **d** Comparison of broadband performance of the three lenses from 20 to 40GHz

frequency. In this section, a number of methods that can be adopted for realizing DCT based antennas are discussed.

The first option is to use sub-wavelength structure arrays, which have been well known as metamaterials [42–44]. This method is able to provide permittivity and/or permeability from negative values to almost infinitely high values, and therefore has been successfully used in many transformation optics-based devices such as the cloak reported in [3] and the carpet cloak reported in Refs. [18, 28]. Generally speaking, a metamaterial unit cell can be either an electric resonator or a magnetic one. For a DCT based antenna device that only requires higher-than-unity permittivities, a large array of electric resonators, for example, the I-shaped resonators, is an efficient option. Figure 7.19a shows a sample of the I-shaped resonator, and Fig. 7.19b illustrates the typical distribution of its effective permittivity. The real part of permittivity (blue curve) follows the Lorentz model, becomes extremely large around the resonance frequency ( $f_r$ ), and changes rapidly. This property indicates an essential disadvantage of resonant metamaterials: narrow-band performance. However, as long as the required relative permittivities are not much higher or much lower than unity, such as in a DCT based antenna design, the resonant metamaterials can operate very well away from the resonance. For example, in Fig. 7.19b the I-shaped resonator has a relatively constant distribution of permittivity value over frequencies much lower than  $f_r$ . Figure 7.19c illustrates how to arrange an array of resonators to mimic a homogeneous block in a permittivity map. Full-wave simulations, the S-parameter retrieval technique [45, 46] and the effective medium theory [47] have been applied to decide the dimensions

**Fig. 7.19** The I-shaped electric resonator.

**a** Dimensions of a unit cell.  
**b** The effective permittivity distribution of I-shaped resonator arrays. *Blue curve*: the real part. *Dashed red curve*: the imaginary part. **c** A group of I-shaped resonators to mimic a homogeneous block in a permittivity map



and arrangement of resonators, as described in Refs. [18, 28]. An advantage of using metamaterials based on printed circuit board (PCB) approaches as shown in Fig. 7.19c is its low cost and readiness for mass-production. The main drawback is that strong spatial and spectral dispersions may occur and therefore limit the bandwidth of the devices.

An alternative method is to drill sub-wavelength holes of different sizes in dielectric host medium. This is the same technology used in the developments of the conventional Fresnel lenses [39, 40] and the recent 3D carpet cloak [48]. These schemes can be regarded as a homogeneous medium replacing the air and the dielectric region. Generally, perforations in the host medium ( $\epsilon_{r1}$ ) lead to a lower relative permittivity value  $\epsilon_{\text{eff}}$  ranging from  $\epsilon_{r2}^{\text{air}}$  to  $\epsilon_{r1}$ . Apparently, several different host media may be needed to fulfill a transformation design corresponding to a required permittivity range. An efficient solution to this problem is to insert high-index dielectric cylinders ( $\epsilon_{r2}^{\text{high}}$ ) into the drilled holes to take place of the air. Therefore, the effective permittivity is expanded to  $\epsilon_{r2}^{\text{air}} < \epsilon_{\text{eff}} < \epsilon_{r2}^{\text{high}}$ . Here we use this method to design the zone plate lens shown in Fig. 7.17 as an example. Figure 7.20 gives the graphical representation of the relationship between the effective permittivity and the perforation. The host material we employ here has a relative permittivity value of  $\epsilon_{r1} = 5.8$  and the filling high index dielectric has a value of  $\epsilon_{r2}^{\text{high}} = 36.7$ . These specific permittivity values are chosen because they are from available dielectrics, and have been successfully applied in the conventional Fresnel lens fabrications [39, 40] and an unidirectional free space cloak design [49]. The effective permittivity can be estimated from the area ratio between the holes ( $\pi d^2/4$ ) and the unit cell ( $l^2$ ) [39, 40]. A more accurate way is to

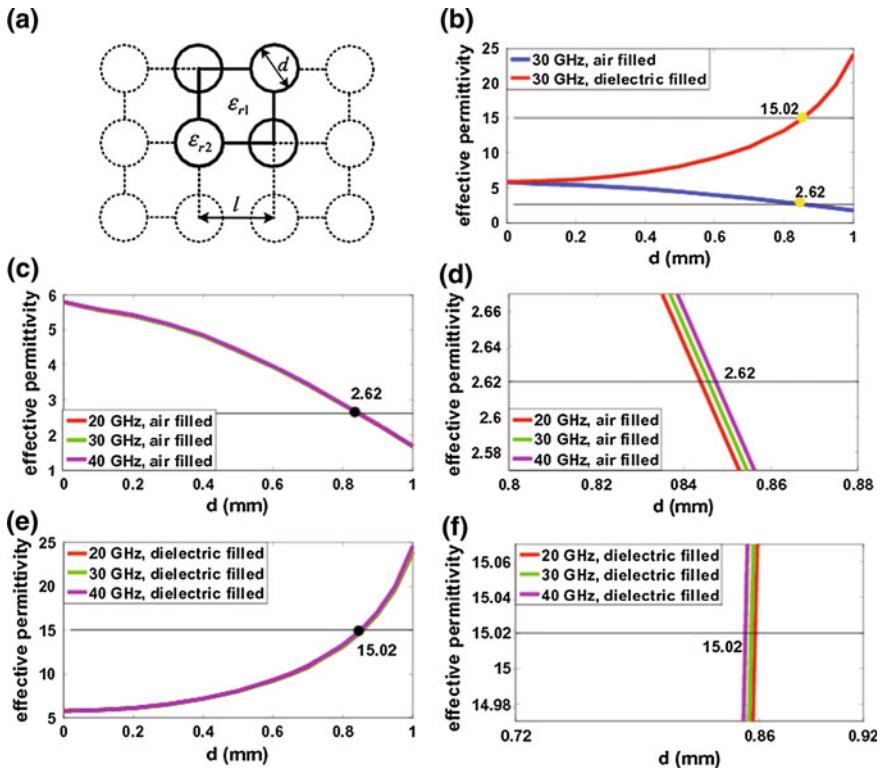


**Fig. 7.20** Graphical representation of the relationship between the effective permittivity and the perforation. The host medium chosen here is  $\epsilon_{r1} = 5.8$ , and the filling material is air  $\epsilon_{r2}^{air} = 1$  or  $\epsilon_{r2}^{high} = 36.7$ .  $d$  refers to the hole diameter, and  $l$  refers to the length of side of the unit cell.  $l = 1$  mm is sub-wavelength scaled in order to make the effective media more homogeneous. **a** Perforated host medium with square unit cell topology. **b** The effective permittivity achieved from the square unit topology at 30 GHz as  $d$  is varied. The maximum value is 24.11, and the minimum value is 1.68. **c** Frequency response of the effective perforated medium from 20 to 40 GHz. **d** Magnified picture of the frequency response in (c) around the effective permittivity equal to 2.62. **e** Frequency response of the perforated medium filled with high dielectric material from 20 to 40 GHz. **f** Magnified picture of the frequency response in (e) around the effective permittivity equal to 15.02. (The curves at different frequencies are very similar, and in (c), (d), (e), (f) clearly overlapped). This represents, for our purposes, dispersionless effective media. The parameter retrieval in (b), (c), (d), (e), and (f) assumes the unit cell to be periodically infinite. In practice, the finiteness of the structure will result in slight changes in effective permittivity)

retrieve the permittivity value from S parameters [46]. Given  $l = 1$  mm, different  $d$  will lead to different effective permittivity, as shown in Fig. 7.20b. As  $d$  varies, the effective permittivity ranges from 1.68 to 24.11. In addition, we can see that the effective permittivity is for our purposes dispersionless, and does not vary much with the frequency as long as the unit cell is sub-wavelength, as shown in Fig. 7.20c–f. Table 7.1 gives the detailed value of  $d$  as a solution to realize the

**Table 7.1** The perforation size ( $d$ ) in every unit cell shown in Fig. 7.20. The unit size is  $l = 1$  mm

$d$ (mm)	1	2	3	4	5	6	7	8	9	10	11
1	0.85	0.83	0.74	0.68	0.59	0.50	0.36	0.19	0.31	0.57	0.76
2	0.52	0.51	0.49	0.46	0.40	0.34	0.15	0.21	0.46	0.66	0.82
3	0.34	0.33	0.31	0.29	0.24	0.14	0.13	0.34	0.52	0.69	0.84
4	0.28	0.28	0.25	0.23	0.16	0.00	0.26	0.36	0.52	0.69	0.85

required permittivity distribution shown in Fig. 7.17c. To be noted, for relative permittivities larger than 5.8, we drill holes and then fill in the high-index dielectric cylinders. In this way, the proposed zone plate lens in Sect. 7.3.3, whose relative permittivity ranges from 2.62 to 15.02, can be completely realized in practice.

Furthermore, the DCT based devices can be realized using non-magnetic and isotropic dielectrics which exhibit only slight dispersion and low loss. These materials are commonly available in nature and are easily controlled and produced. For demonstrating purpose, here we present an all-dielectric design of a carpet cloak that reported in [19].

To begin with, a carpet cloak is designed in [50], and the permittivity map is down-sampled to six dielectric blocks as shown in Fig. 7.21, with refractive indexes of 1.08, 1.14 and 1.21, corresponding to relative permittivities of 1.17, 1.30 and 1.46. These dielectrics are located around a metallic perturbation that is

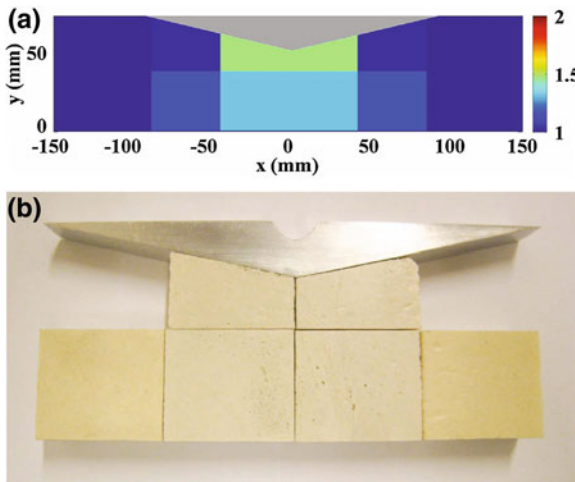


**Fig. 7.21** The perturbation bounded by the composite dielectrics. The perturbation is an aluminium triangle of height 16 mm and base 144 mm. At the base of the triangle is a metal boundary. In **a**, the dielectric 2D map of the  $4 \times 2$  blocks is shown. The dielectric blocks are rectangles of dimension  $34.25 \times 30$  mm<sup>2</sup>. The fabricated cloak is shown in **(b)**. In practice, a metallic ground plane is located at the base of the triangular perturbation, while the entire structure is enclosed within parallel metallic plates



to be ‘hidden’ from the incident electromagnetic waves. The dielectric blocks have a size of  $34.25 \times 30 \text{ mm}^2$  ( $1.14\lambda \times \lambda$  at 10 GHz), with the dielectric blocks in contact with the perturbation cut appropriately as shown in Fig. 7.21. The perturbation is an electrically large aluminium triangle with a base of 144 mm and a height of 16 mm ( $b = 4.8\lambda$  and  $h = 0.53\lambda$  at 10 GHz). At the base of the triangle is a metallic ground plane. The fabricated cloak is shown in Fig. 7.21b.

The first stage in the realization of the cloak is the development and full characterization of the dielectric mixtures. The requirements for the composing materials of each block are that they exhibit low loss and low dispersion at microwave frequencies. Homogeneous composites of polyurethane and ceramic particles are required, with strong bonding between ceramic particles and the polymer matrix, and reasonably good mechanical properties. Additionally, composites with the requisite range of dielectric properties must be easily fabricated on demand. Accordingly, a dielectric mixture of polyurethane with high- $\kappa$  barium titanate ( $\text{BaTiO}_3$ ) is found to be suitable for this purpose. Polyurethane is used to create a low- $\kappa$  foam matrix, and  $\text{BaTiO}_3$  is used to load the foam in order to increase the effective permittivity while not greatly altering the mechanical properties of the structure. The density of  $\text{BaTiO}_3$  powder is low, and the small particle size is advantageous when used in a dispersion system and is less likely to affect the polymer matrix structure. This results in less damage to the mechanical properties of the composite material. Both substances exhibit low loss and low dispersion at microwave frequencies, and are thus suitable for our requirements.

A range of  $\text{BaTiO}_3$  / polyurethane composites were fabricated to realize the required permittivity values by changing the  $\text{BaTiO}_3$  particle loading. The relative permittivity of the composite at 1 MHz and 10 GHz are measured and plotted in Fig. 7.22. The measured permittivities show very good agreement with the specified values, with errors of up to about 2 %. Furthermore, as the measured permittivities at both frequencies agree relatively well, it would imply that there is

**Fig. 7.22** Measured relative permittivity versus  $\text{BaTiO}_3$  volume fraction of the  $\text{BaTiO}_3$ /polyurethane composite, at 1 MHz and 10 GHz. Measured points are plotted and compared with the Maxwell-Garnett ( $\cdots$ ) and Bruggeman ( $---$ ) effective medium relationships for three-phase mixtures

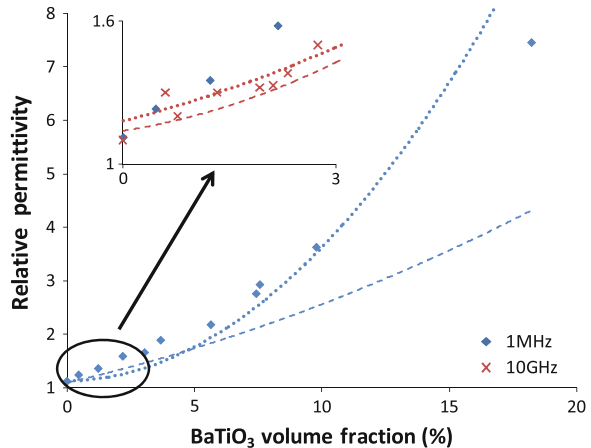
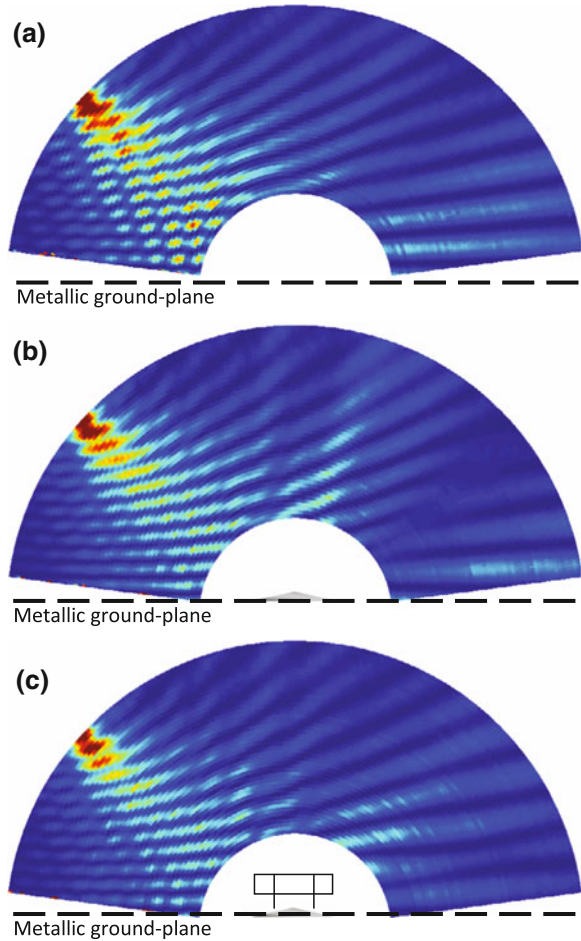


**Fig. 7.23** Measured electric fields. The electric fields measured in the near-field scanning system are shown. Due to the setup of the scanning system, the semicircular region in which the perturbation and cloak are placed cannot be scanned and is left blank. **a** The empty system (no perturbation or cloak), showing only the incident wave reflecting off of the metallic ground plane. **b** The perturbation resting on the ground plane. **c** The cloaked perturbation. Strong scattering is evident with the perturbation. The cloak significantly reduces the scattering due to the perturbation, with the resulting field distribution similar to that of the perturbation-free system



little dispersion between the bands. It is clear that a large range of permittivity values can be attained by controlling the volume percentage of  $BaTiO_3$ .

A prototype of the all-dielectric carpet cloak is measured in a near-field scanner system which operates at frequencies between 6 and 12 GHz. It is composed of two parallel conducting plates, each with a diameter of 1 m and spaced 15 mm apart. Holes have been drilled in the top plate, which rotates at intervals that give a resolution of 5 mm. A monopole measures the fields between the two plates at each interval, while a wave is incident from a fixed X-band waveguide (single-mode operational frequency range: 8.2 to 12.4 GHz; cutoff frequency: 6.557 GHz). Details of the measurement setup is described in [19]. Figure 7.23 shows the measured electric fields inside the near-field scanner system. Firstly, the near-field scanner is tested with an empty setup. The measured 2D field amplitude plot is shown in Fig. 7.23a, with the well-formed wavefronts visible. Figure 7.23b represents the measured fields when the perturbation has been introduced. In this case,

the effect on the incoming wave is clearly evident, with scattering and diffraction leading to at least two visibly separate paths of the reflected waves. The goal of the carpet cloak is to ‘hide’ the electrically large metallic perturbation; reconstructing the scattered waves so that they appear identical to those of the empty scanner. To accomplish this, the dielectric materials are ordered around the object, as illustrated in Fig. 7.21b. In the measurement shown in Fig. 7.23c, it is clear that, in contrast to the perturbed case, the scattered fields appear less affected by the block; the two separate scattered beams are no longer visible, and the wavefront profile appears very similar to that of the empty scanner. In conclusion, the carpet cloak composed of only six dielectric blocks does function to ‘hide’ the perturbation.

## 7.5 Summary

In this chapter, the discrete coordinate transformation (DCT) was introduced as a practical implementation of the transformation electromagnetics to create all-dielectric antennas. It was demonstrated in theory that under certain orthogonal conditions, this method can lead to transformation devices composed of isotropic and non-magnetic dielectrics. Due to this property, the discrete coordinate transformation is extremely suitable for the design of broadband antennas with compact volumes, flexible profiles and even custom-projected electromagnetic performances, as well as specifying designs that are easy to fabricate. Several broadband antenna devices, including a flat reflector, a flat lens, and a zone plate Fresnel lens were designed and numerically validated as examples. In addition, three different realization methods for DCT based designs were discussed and demonstrated.

## References

1. Leonhardt U (2006) Optical conformal mapping. *Science* 312:1777–1780
2. Pendry JB, Schurig D, Smith DR (2006) Controlling electromagnetic fields. *Science* 312:1780–1782
3. Schurig D, Mock JJ, Justice BJ, Cummer SA, Pendry JB, Starr AF, Smith DR (2006) Metamaterial electromagnetic cloak at microwave frequencies. *Science* 314:977–980
4. Cai W, Chettiar UK, Kildishev AV, Shalaev VM (2007) Optical cloaking with metamaterials. *Nature Photon* 1:224–227
5. Jiang WX, Chin JY, Li Z, Cheng Q, Liu R, Cui TJ (2008) Analytical design of conformally invisible cloaks for arbitrarily shaped objects. *Phys Rev E* 77:066607
6. Alù A, Engheta N (2008) Multifrequency optical invisibility cloak with layered plasmonic shells. *Phys Rev Lett* 100:113901
7. Luo Y, Chen H, Zhang J, Ran L, Kong JA (2008) Design and analytical full-wave validation of the invisibility cloaks, concentrators, and field rotators created with a general class of transformations. *Phys Rev B* 77:125127
8. Chen H, Hou B, Chen S, Ao X, Wen W, Chan CT (2009) Design and experimental realization of a broadband transformation media field rotator at microwave frequencies. *Phys Rev Lett* 102:183903

9. Rahm M, Schurig D, Roberts DA, Cummer SA, Smith DR, Pendry JB (2008) Design of electromagnetic cloaks and concentrators using form-invariant coordinate transformations of Maxwell's equations. *Photon Nanostruct Fundam Appl* 6:87–95
10. Yaghjian AD, Maci S (2008) Alternative derivation of electromagnetic cloaks and concentrators. *New J Phys* 10:115022
11. Jiang WX, Cui TJ, Cheng Q, Chin JY, Yang XM, Liu R, Smith DR (2008) Design of arbitrarily shaped concentrators based on conformally optical transformation of nonuniform rational B-spline surfaces. *Appl Phys Lett* 92:264101
12. Alù A, Engheta N (2009) Cloaking a sensor. *Phys Rev Lett* 102:233901
13. Narimanov EE, Kildishev AV (2009) Optical black hole: Broadband omnidirectional light absorber. *Appl Phys Lett* 95:041106
14. Cheng Q, Cui TJ, Jiang WX, Cai BG (2010) An omnidirectional electromagnetic absorber made of metamaterials. *New J Phys* 12:063006
15. Kong F, Wu B, Kong JA, Huangfu J, Xi S, Chen H (2007) Planar focusing antenna design by using coordinate transformation technology. *Appl Phys Lett* 91:253509
16. Kundtz N, Smith DR (2009) Extreme-angle broadband metamaterial lens. *Nat Mater* 9:129–132
17. Li J, Pendry JB (2008) Hiding under the carpet: A new strategy for cloaking. *Phys Rev Lett* 101:203901
18. Liu R, Ji C, Mock JJ, Chin JY, Cui TJ, Smith DR (2009) Broadband ground-plane cloak. *Science* 323:366–369
19. Bao D, Rajab KZ, Hao Y, Kallos E, Tang W, Argyropoulos C, Piao Y, Yang S (2011) All-dielectric invisibility cloaks made of BaTiO<sub>3</sub>-loaded polyurethane foam. *New J Phys* 13:103023
20. Valentine J, Li J, Zentgraf T, Bartal G, Zhang X (2009) An optical cloak made of dielectrics. *Nat Mater* 8:568–571
21. Gabrielli LH, Cardenas J, Poitras CB, Lipson M (2009) Silicon nanostructure cloak operating at optical frequencies. *Nature Photon* 3:461–463
22. Thompson JF, Soni BK, Weatherill NP (1999) *Handbook of grid generation*. CRC Press, Boca Raton
23. Holland R (1983) Finite-difference solution of maxwell's equations in generalized nonorthogonal coordinates. *IEEE Trans Nucl Sci* 30:4589–4591
24. Hao Y, Railton CJ (1998) Analyzing electromagnetic structures with curved boundaries on Cartesian FDTD meshes. *IEEE Trans Microwave Theory Tech* 46:82–88
25. Pozar DM (2005) *Microwave engineering*, 3rd edn. Wiley, London
26. Tang W, Argyropoulos C, Kallos E, Song W, Hao Y (2010) Discrete coordinate transformation for designing all-dielectric flat antennas. *IEEE Trans Ant Propag* 58:3795–3804
27. Mesh and grid generation software for CFD - Pointwise. <http://www.pointwise.com/>
28. Ma HF, Jiang WX, Yang XM, Zhou XY, Cui TJ (2009) Compact-sized and broadband carpet cloak and free-space cloak. *Opt Express* 17:19947–19959
29. Kallos E, Argyropoulos C, Hao Y (2009) Ground-plane quasicloaking for free space. *Phys Rev A* 79:63825
30. Shannon CE (1949) Communication in the presence of noise. *Proc IRE* 37:10–21
31. Taflove A, Hagness SC (2005) *Computational electrodynamics : the finite-difference time-domain method*, 3rd edn. Artech House, London
32. Hao Y, Mittra R (2009) *FDTD modeling of metamaterials: theory and applications*. Artech House, London
33. Zhao Y, Argyropoulos C, Hao Y (2008) Full-wave finite-difference time-domain simulation of electromagnetic cloaking structures. *Opt Express* 16:6717–6730
34. Argyropoulos C, Zhao Y, Hao Y (2009) A radially-dependent dispersive finite-difference time-domain method for the evaluation of electromagnetic cloaks. *IEEE Trans Ant Propag* 57:1432–1441

35. Yan M, Ruan Z, Qiu M (2007) Scattering characteristics of simplified cylindrical invisibility cloaks. *Opt Express* 15:17772–17782
36. HFSS: 3D full-wave electromagnetic field simulation. <http://www.ansoft.com/products/hf/hfss>
37. Loewen EG, Popov E (1997) *Diffraction gratings and application*. Marcel Dekker, New York
38. Hristov HD (2000) *Fresnel zones in wireless lines, zone plate lenses and antennas*. Wrtech House, London
39. Petosa A, Ittipiboon A (2003) Design and performance of a perforated dielectric Fresnel lens. *IEE Proc Microw Antennas Propag* 150:309–314
40. Petosa A, Ittipiboon A, Thirakoune S (2006) Investigation on arrays of perforated dielectric Fresnel lenses. *IEE Proc Microw Antennas Propag* 153:270–276
41. Yang R, Tang W, Hao Y (2011) A broadband zone plate lens from transformation optics. *Opt Express* 19:12348–12355
42. Pendry JB, Holden AJ, Stewart WJ, Youngs I (1996) Extremely low frequency plasmons in metallic mesostructures. *Phys Rev Lett* 76:4773–4776
43. Pendry JB, Holden AJ, Robbins DJ, Stewart WJ (1999) Magnetism from conductors and enhanced nonlinear phenomena. *IEEE Trans Micr Theory Techn* 47:2075–2084
44. Schurig D, Mock JJ, Smith DR (2006) Electric-field-coupled resonators for negative permittivity metamaterials. *Appl Phys Lett* 88:041109
45. Smith DR, Schultz S, Markoš P, Soukoulis CM (2002) Determination of effective permittivity and permeability of metamaterials from reflection and transmission coefficients. *Phys Rev B* 65:195104
46. Smith DR, Vier DC, Koschny Th, Soukoulis CM (2005) Electromagnetic parameter retrieval from inhomogeneous metamaterials. *Phys Rev E* 71:036617
47. Smith DR, Pendry JB (2006) Homogenization of metamaterials by field averaging. *J Opt Soc* 23:391
48. Ma HF, Cui TJ (2010) Three-dimensional broadband ground-plane cloak made of metamaterials. *Nat Commun* 1:21
49. Bao D, Kallos E, Tang W, Argyropoulos C, Hao Y, Cui TJ (2010) A broadband simplified free space cloak realized by nonmagnetic dielectric cylinders. *Front Phys China* 5:319–323
50. Kallos E, Argyropoulos C, Hao Y (2009) Ground-plane quasicloaking for free space. *Phys Rev A* 79:63825